Supplementary Information

AMS Calibrations for UWFPS

Normal procedures were used to calibrate the AMS flow rate as a function of measured lens pressure and particle time-of-flight velocity as a function of particle size [*Canagaratna et al.*, 2007]. For airborne measurements, we used a pressure-controlled inlet (PCI) that maintained a constant mass flow rate into the AMS [*Bahreini et al.*, 2008]. Because particle velocity depends on the AMS flow rate [*Bahreini et al.*, 2003], the PCI also provided a stable velocity calibration. The flow rate and velocity calibration values used for UWFPS were similar to those found for our other studies with the same AMS instrument operated with the PCI. The actual sampling pressures for both the PCI and the AMS inlet were recorded and remained constant.

For nitrate ionization efficiency (IE_{NO3}) calibrations, the ion signals from individual, size-selected, ammonium nitrate particles are used to determine the number of ions per unit mass generally in the following manner. Dry ammonium nitrate particles are formed by nebulizing a dilute aqueous solution with a custom atomizer followed by a silica gel dryer. These particles then sized with a calibrated differential mobility analyzer (DMA), ranging from about 250 nm to 500 nm in mobility diameter. Individual particle mass spectra are recorded with the AMS for at least 200 individual particle events at each size. For each particle spectrum recorded, the main nitrate ion signals at *m/z* 30 and 46 are integrated to obtain the number of nitrate ions per particle for a given mass obtained by converting the mobility diameter into volume and applying the particle density and Jayne shape factor [*Jayne et al.*, 2000]. The number of *m/z* 30 plus 46 ions per molecule of ammonium nitrate is the definition of IE_{NO3} and is subsequently used to convert ion signals from the AMS into mass units [*J.D. Allan et al.*, 2003]. This procedure relies on a narrow size range obtained from a calibrated DMA.

Here we used a slightly different procedure to determine IE_{NO3}. Instead of stepping through sizes with the DMA with a narrow size window, we increased the size range of particles transmitted through the DMA and used the AMS internal size calibration of vacuum aerodynamic diameter (d_{va}) from the particle time-of-flight velocity to calculate the particle size with the AMS. Plots of the integrated ion signals per particle (IPP) versus the cube of the vacuum aerodynamic diameter (d_{va}^3 in nm^3) are linear as shown below for calibration data obtained on 23 Jan. 2017.

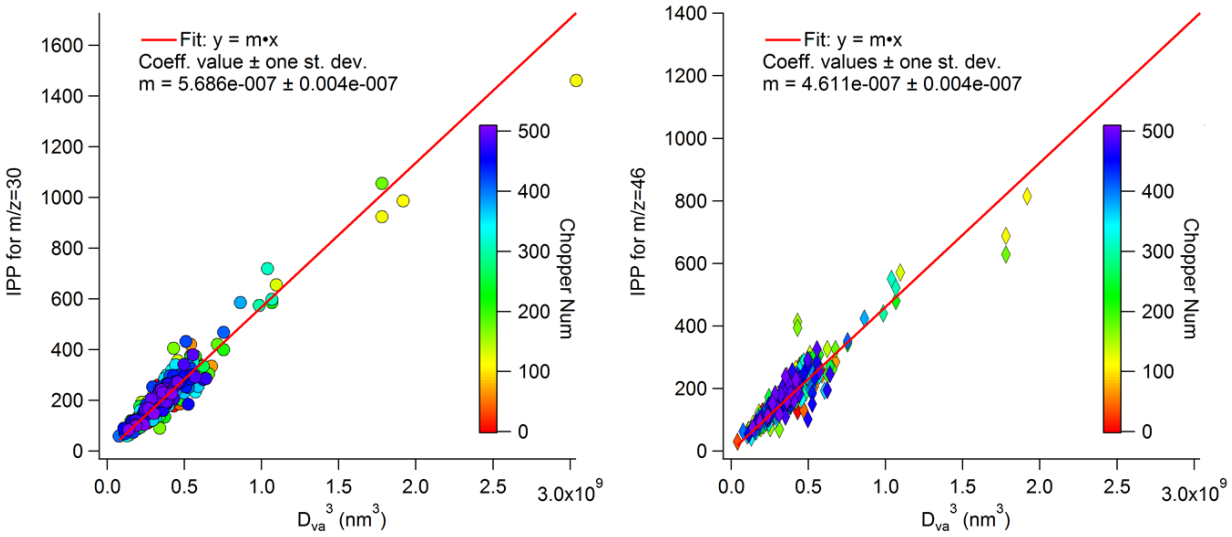

Points are colored by particle number and do not indicate any dependence with time over a wide range of particle volumes. Linear regression fits are shown with the intercept coefficients forced through zero. The vacuum aerodynamic diameter is proportional to the physical diameter times the effective density [*DeCarlo et al.*, 2004], and so the cube of the vacuum aerodynamic diameter is a measure of particle volume. Hence, d_{va}^3 for each particle can be converted into units of mass per particle. Therefore the sum of the two slopes from these plots are proportional to IE_{NO3} as follows:

$$IE_{NO3} = [IPP_{slope\ at\ 30} + IPP_{slope\ at\ 46}] \times 6/\pi \times MW_{NH4NO3} \times (s \times \rho_{NH4NO3})^2 / (N_A\ \rho_0^3\ 10^{-21}) \quad (1)$$

where the value of 10^{-21} is a unit conversion factor for nm^3 to cm^3. Using the molecular weight of ammonium nitrate (MW_{NH4NH3} = 80 g mol^{-1}), the Jayne shape factor for ammonium nitrate (s = 0.8 [*Jayne et al.*, 2000]), the density of dry ammonium nitrate (ρ_{NH4NO3} = 1.72 g cm^{-3} [*Perry and Green*, 1997]), Avogadro's number (N_A = 6.022e23 molec mol^{-1}), standard density (ρ_0 = 1 g cm^{-3}), and π = 3.14, this equation simplifies to:

$$IE_{NO3} = [IPP_{slope\ at\ 30} + IPP_{slope\ at\ 46}] \times 0.48 \quad (2)$$

where IE_{NO3} is in units of ions per molecule. This procedure eliminates issues with calibrating the DMA and has the advantage of using the internal AMS sizing calibration to independently determine IE_{NO3}.

For IE_{NO3} calibrations encompassing the entire UWFPS study, we found that the ratio of IE_{NO3} to the airbeam signal at *m/z* 28 (AB) was linear over a wide range of sensitivities.

$$IE_{NO3} = 1.167e\text{-}12 \times AB - 2.06e\text{-}7 \quad (3)$$

This equation was used to calculate IE_{NO3} for a reference AB value at the beginning of each set of flights on a given day.

The relative ionization efficiency of ammonium (RIE_{NH4}) was determined from all of the ammonium nitrate calibration data by forcing the number of moles from the measured ammonium ion signals equal to the number of moles from the measured nitrate ion signals for the ammonium nitrate particles. It had a slight time dependence over the course of the study, decreasing from 4.46 on 31 Dec. 2016 to 3.44 on 2 Feb. 2017.For the final calibration on 10 Feb. 2017, RIE_{NH4} was 3.42.

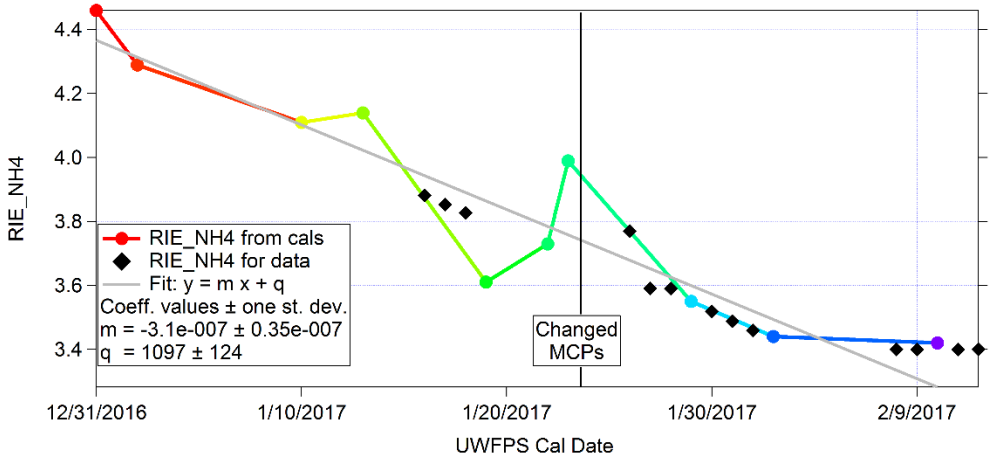

This time dependence in the RIE_{NH4} calibrations (colored points) was fit to the following equation (grey line above):

$$RIE_{NH4} = -3.0636e\text{-}7 \times (\text{date in seconds}) + 1097 \quad (4)$$

and used for the UWFPS data with the minimum RIE_{NH4} for the last 4 flights fixed at 3.4.

If complete ion balance is assumed for the ambient UWFPS measurements (during polluted conditions the inorganic NR-PM_1 composition was mostly ammonium nitrate, see Figures 3, 4, S6, and S7), an implied RIE_{NH4} can be determined from the field data (black diamonds above). The overall trend in time for RIE_{NH4} measured from the calibrations was clearly evident in the ambient data and the nearly constant RIE_{NH4} of 3.4 at the end of the study was seen in both the calibrations and ambient data. Even a slightly higher

RIE_{NH4} was reflected in the ambient data for the flight directly after changing the microchannel plate detectors (MCPs) in the middle of the study. Thus, this careful calibration of RIE_{NH4} demonstrates the overall ion balance to within a few percent in the UWFPS dataset (see Figure 5 in the main text).

For the final calculation of the mass concentrations, the collection efficiency (CE) must be determined [*J. D. Allan et al.*, 2004; *Matthew et al.*, 2008]. Here the bulk inorganic speciation was used to initially estimate CE using the algorithm based on prior field data [*Middlebrook et al.*, 2012], and indicated that it should be less than one for most of this dataset. However, the instrument used for this study has a light scattering (LS) module to measure the in situ CE of particles that are large enough to scatter light [*Liao et al.*, 2017]. We operated the instrument in the light scattering single particle mode for 30 s every 5 minutes. During time periods where significant mass concentrations of ammonium nitrate were measured, the in situ CE from light scattering was closer to 1 than indicated from the CE algorithm. Because CE from the LS counts was closer to 1 and CE for pure, dry ammonium nitrate equals 1 [*Matthew et al.,* 2008], we used CE = 1 for most of this dataset.

There is some uncertainty in CE for the smallest mass concentrations, where the particle counting statistics were not high enough to reliably use the in situ CE from light scattering data. The mass fraction data as a function of total AMS mass indicated that the composition was clearly different than for the higher total mass concentrations (see Figure 3, 4 and S5), and the CE could potentially also be different. There is also uncertainty in the CE for data points where the refractory chloride mass fraction was relatively high, typically for measurements around the magnesium plant on the southwestern side of the Great Salt Lake. For those data points with low total mass concentrations or high chloride mass fractions, we assumed that the CE was also equal to 1. However, the true CE could be as low as 0.3. Hence, the mass concentrations in the data archive for these data points should be considered a lower limit and could actually be as much as a factor of 2 or 3 larger than reported.

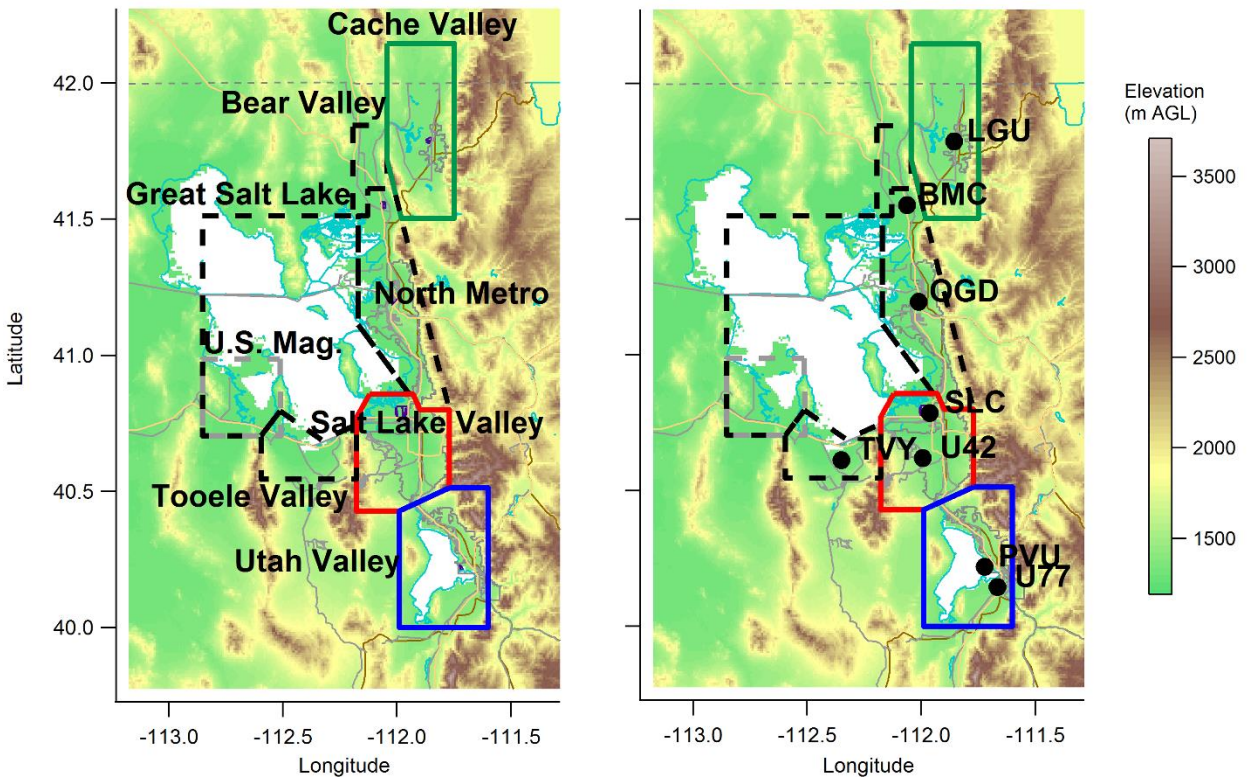

Figure S1. Maps of the area of interest for our study. Left: Outlines of the boundaries for the regions considered in our analysis. From north to south: Cache Valley, Bear Valley, Great Salt Lake, North Metro, U.S. Magnesium plant, Salt Lake Valley, Tooele Valley and Utah Valley. Right: location of the airports where we performed missed approaches in order to measure vertical profiles. From north to south and from left to right: Logan-Cache Airport (LGU), Brigham City Airport (BMC), Ogden-Hinckley Airport (OGD), Salt Lake City International Airport (SLC), Tooele Valley Airport (TVY), South Valley Regional Airport (U42), Provo Municipal Airport (PVU) and Spanish Fork Springville (U77). The dashed lines are the same boundaries of the air basins as the left panel.

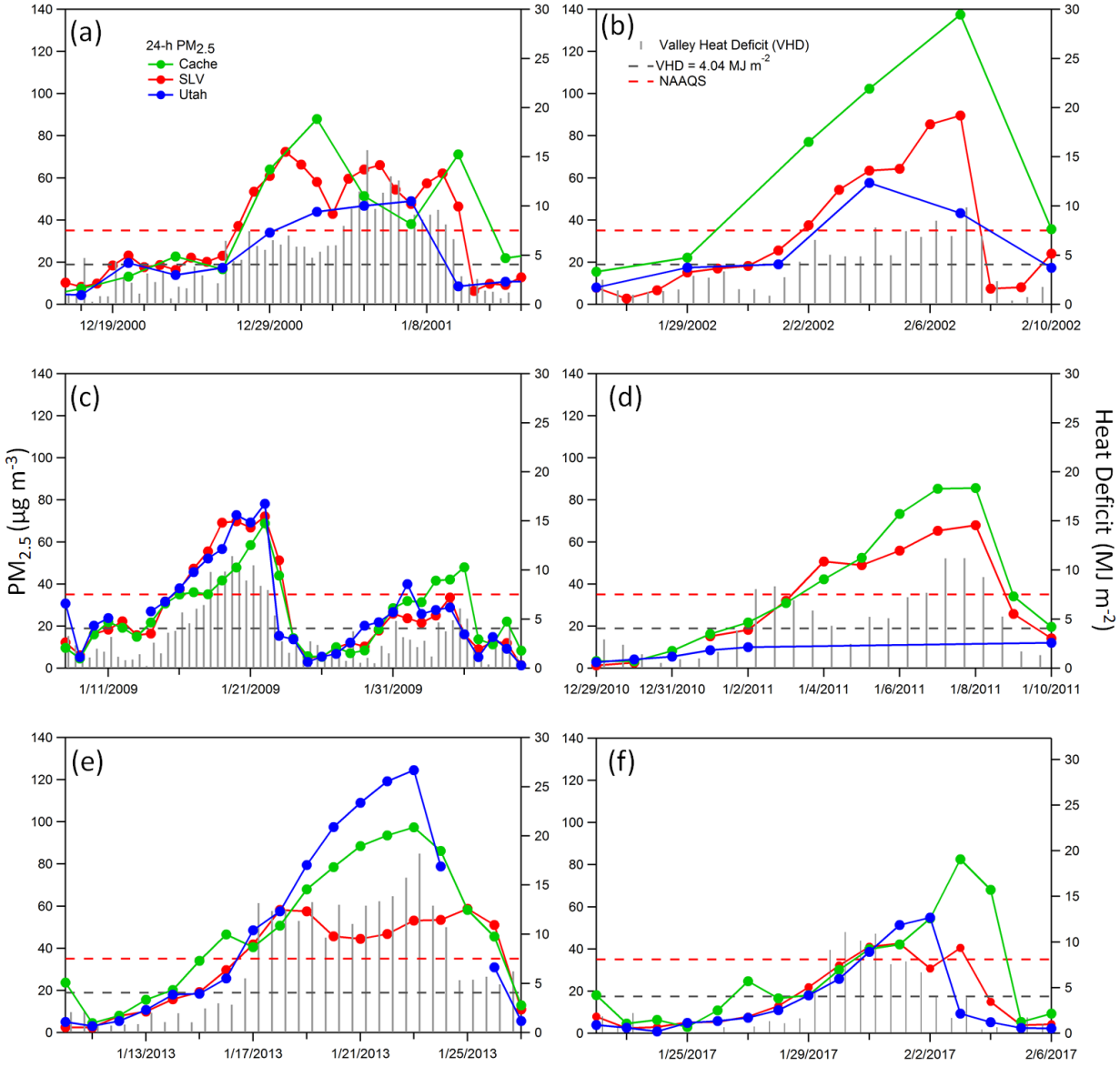

Figure S2. Examples showing the evolution of $PM_{2.5}$ during the winter with long-lasting episodes that occurred in years prior to UWFPS (a to e) and during UWFPS (f). The grey sticks are the valley heat deficit (VHD) values calculated following Whiteman et al. (2014), using data from balloon soundings at the Salt Lake City International Airport. High VHD values are characteristic of persistent cold air pools (PCAPs), where pollutants are trapped near the ground. The grey dashed horizontal lines are the threshold of 4.04 MJ m^{-2} (Whiteman et al. 2014) and the red dashed horizontal lines are the National Ambient Air Quality Standard (NAAQS) for 24-h average $PM_{2.5}$

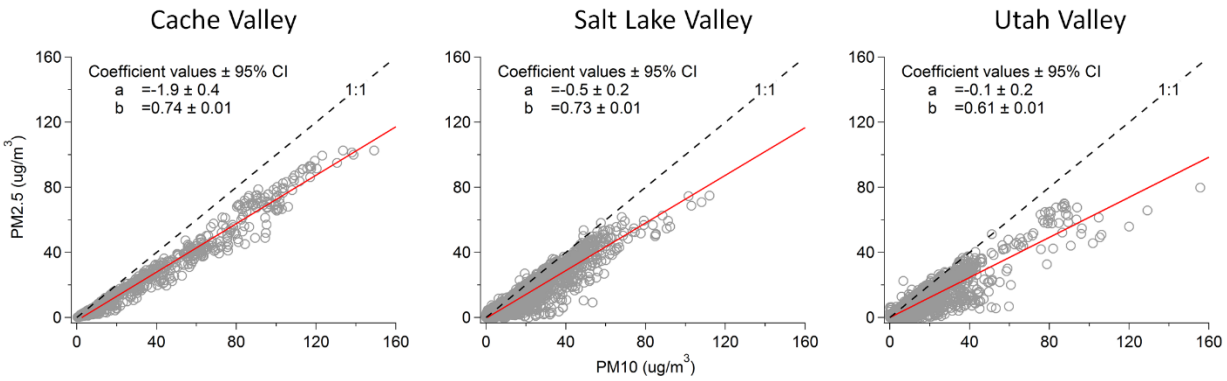

Figure S3. Comparison between hourly PM_{10} and $PM_{2.5}$ for three of the locations considered in this study. Left: Cache Valley, data from the Logan L4 site (Environmental Protection Agency). Center: Salt Lake Valley, data from the Hawthorn site (Utah Division of Air Quality –UDAQ). Right: Utah Valley, data from the North Provo site (UDAQ). The grey dashed lines are the 1:1 line; the red solid lines are linear fit. At the top of each graph are the intercepts (a) the slopes (b) from linear fits, with 95% confidence intervals (CI).

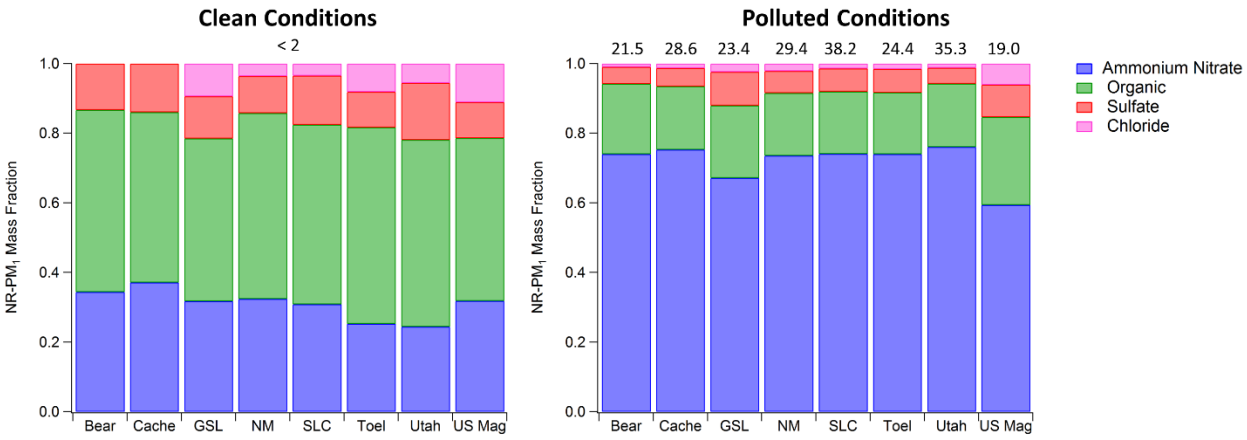

Figure S4. Average aerosol chemical composition (calculated as non-refractory PM_1 mass fraction) measured from the Twin Otter during UWFPS outside pollution events (i.e., when the total mass was less than 2 µg m^{-3}–left) and during pollution events (i.e., when the total mass was greater than 17.5 µg sm^{-3}–. The values above the bar charts are median concentrations for polluted conditions over the entire period of the UWFPS.

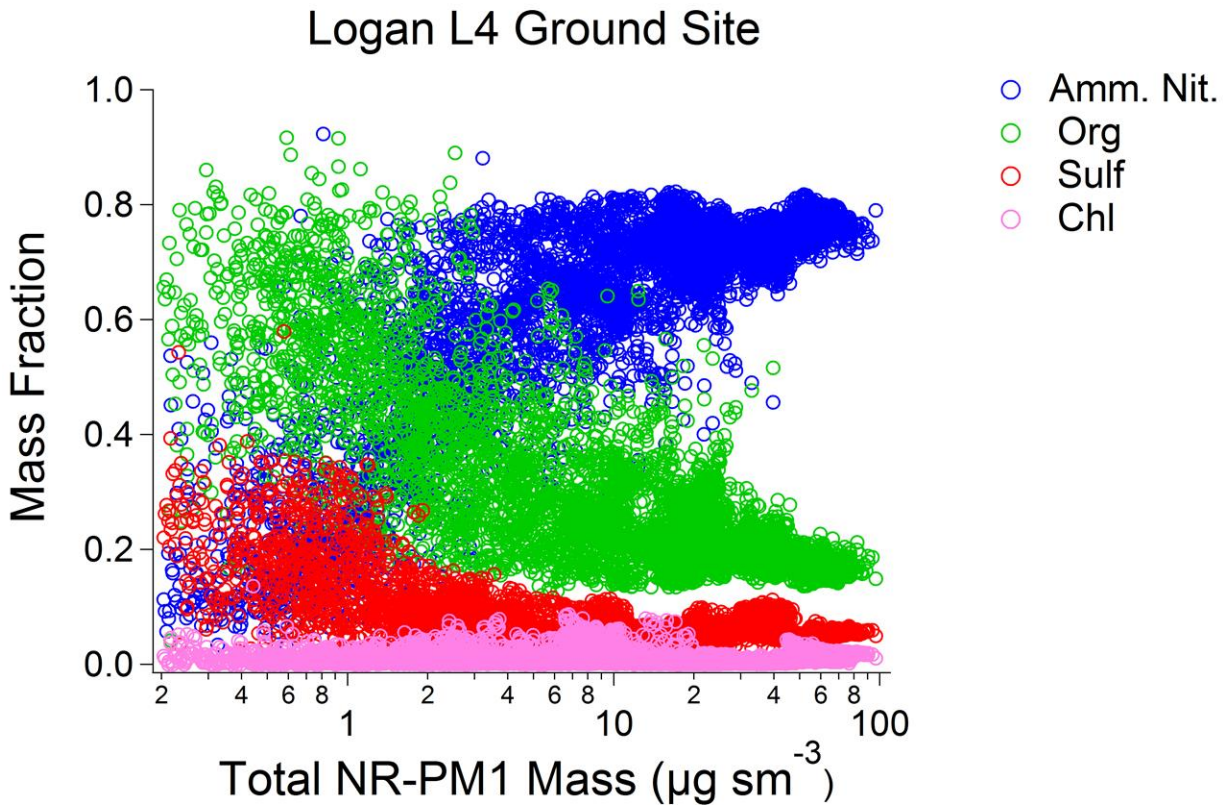

Figure S5. Aerosol mass fraction as a function of the total mass of NR-PM_1. Data from the AMS located at the Logan L4 ground site. The mass fraction of ammonium nitrate is in blue, of organic in green, of sulfate and chloride in red and pink, respectively.

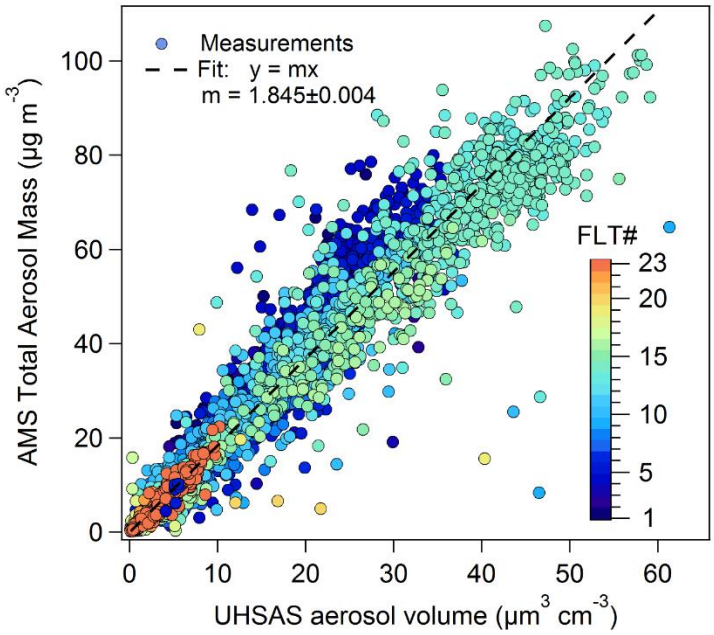

Figure S6. Comparison between the total aerosol mass in µg m^{-3}, measured with the AMS and the aerosol volume in μm^3 cm^{-3}, measured with the UHSAS. The black dashed line is a fit through the data. The slope, *m* = 1.85, is within experimental error compatible with the density of ammonium nitrate (1.72 g cm^{-3}, NIST Chemistry WebBook). Color-coded is the flight number.

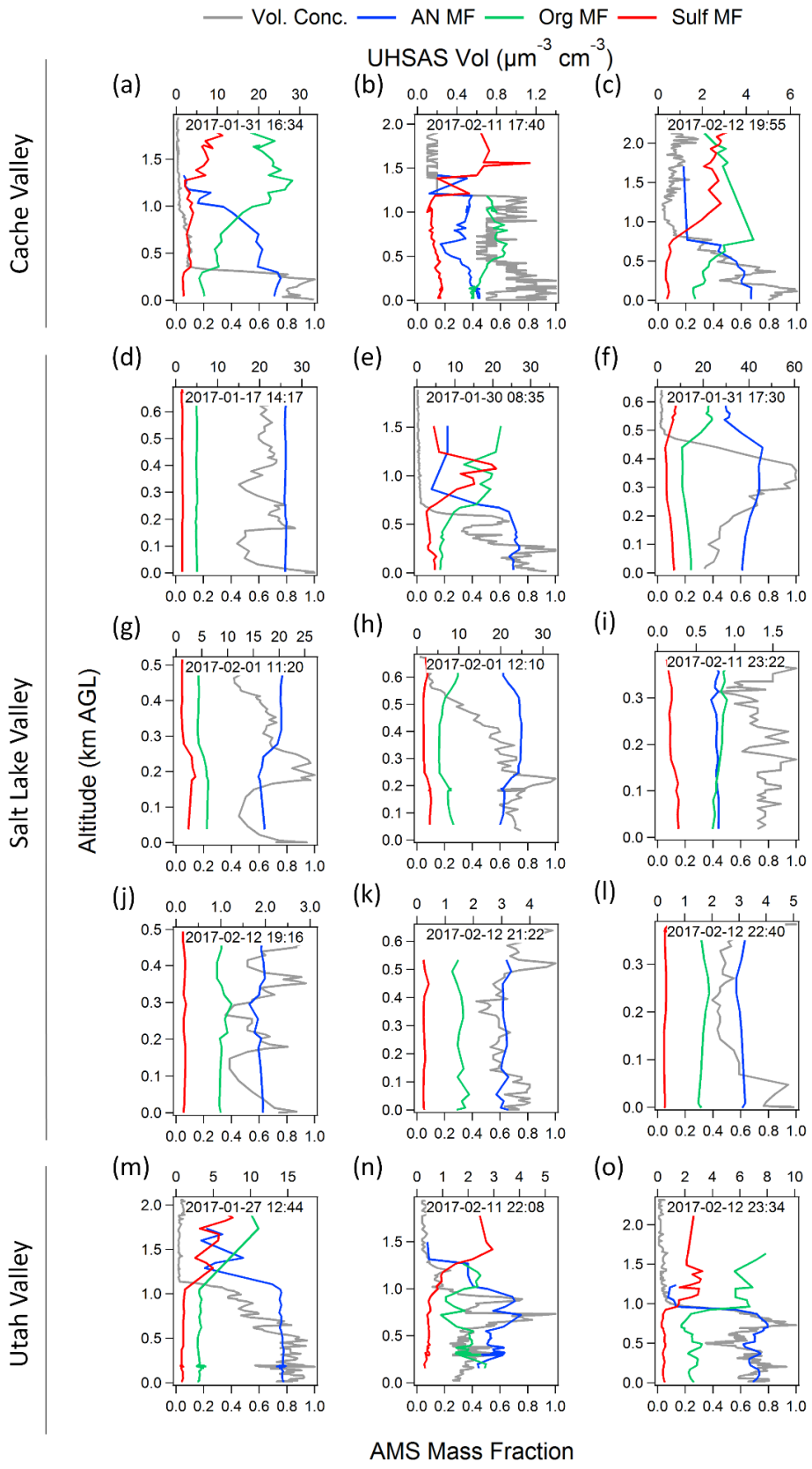

Figure S7. Various vertical profiles of aerosol volume (top axis) and aerosol NR-PM_1 mass fraction (bottom axis) for Cache Valley, Salt Lake valley and Utah Valley.

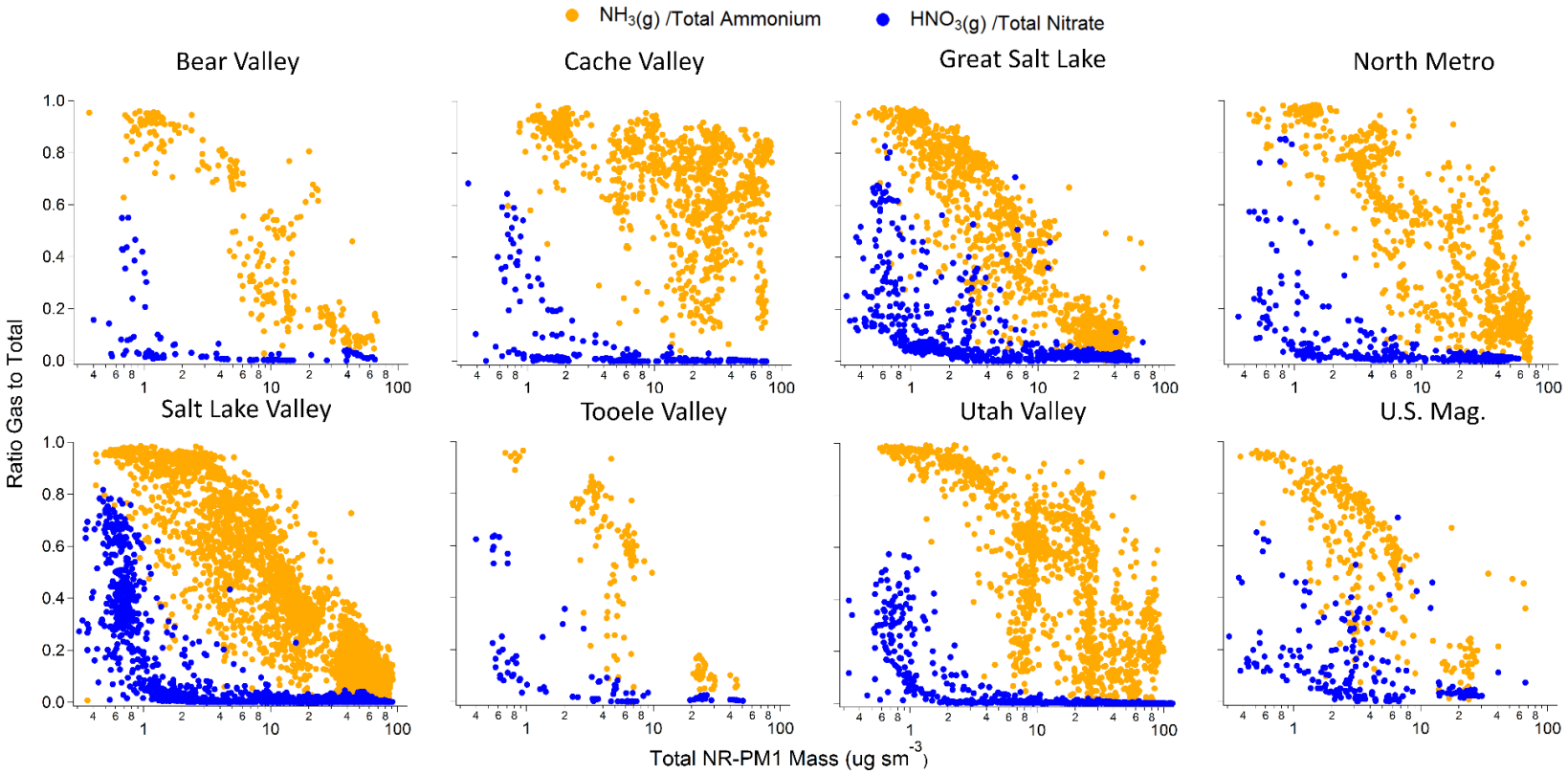

Figure S8. Fraction of gas phase species to total mass (gas + aerosol) plotted as a function of total aerosol mass. Same as figure 9 in the main text, only for all the regions.

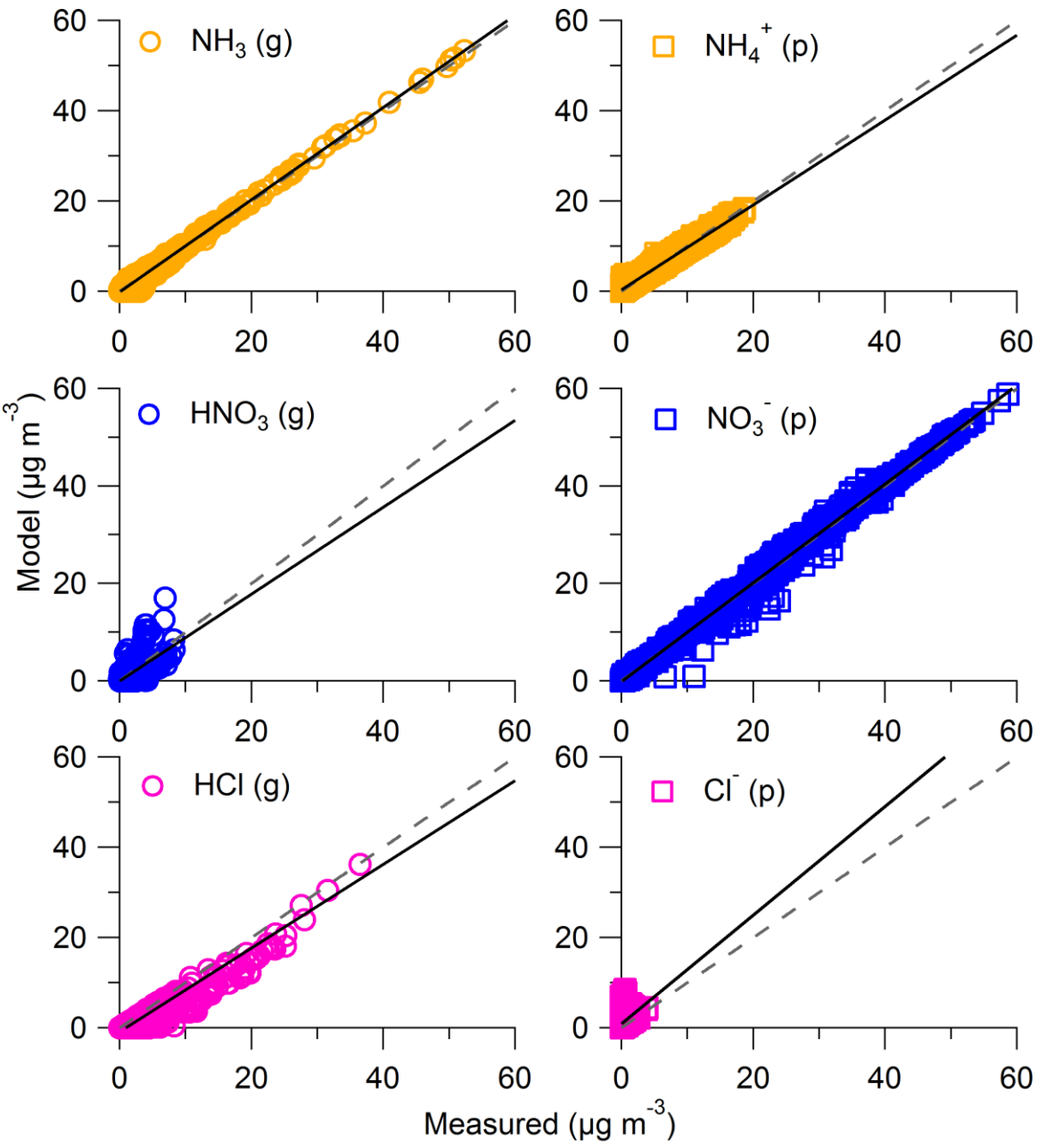

Figure S9. Comparison between measurements and ISORROPIA model output. The gas phase species denoted by "(g)", are in the left column and the particle phase species, denoted by "(p)", are in the right column. Ammonia (NH_3) and ammonium (NH_4^+) are in yellow at the top, nitric acid (HNO_3) and nitrate (NO_3^-) are in blue at the center, hydrochloric acid (HCl) and chloride (Cl^-) are in pink at the bottom. The grey dashed line is the 1:1 line, the solid black lines are linear regressions (see Table S1 for the coefficients).

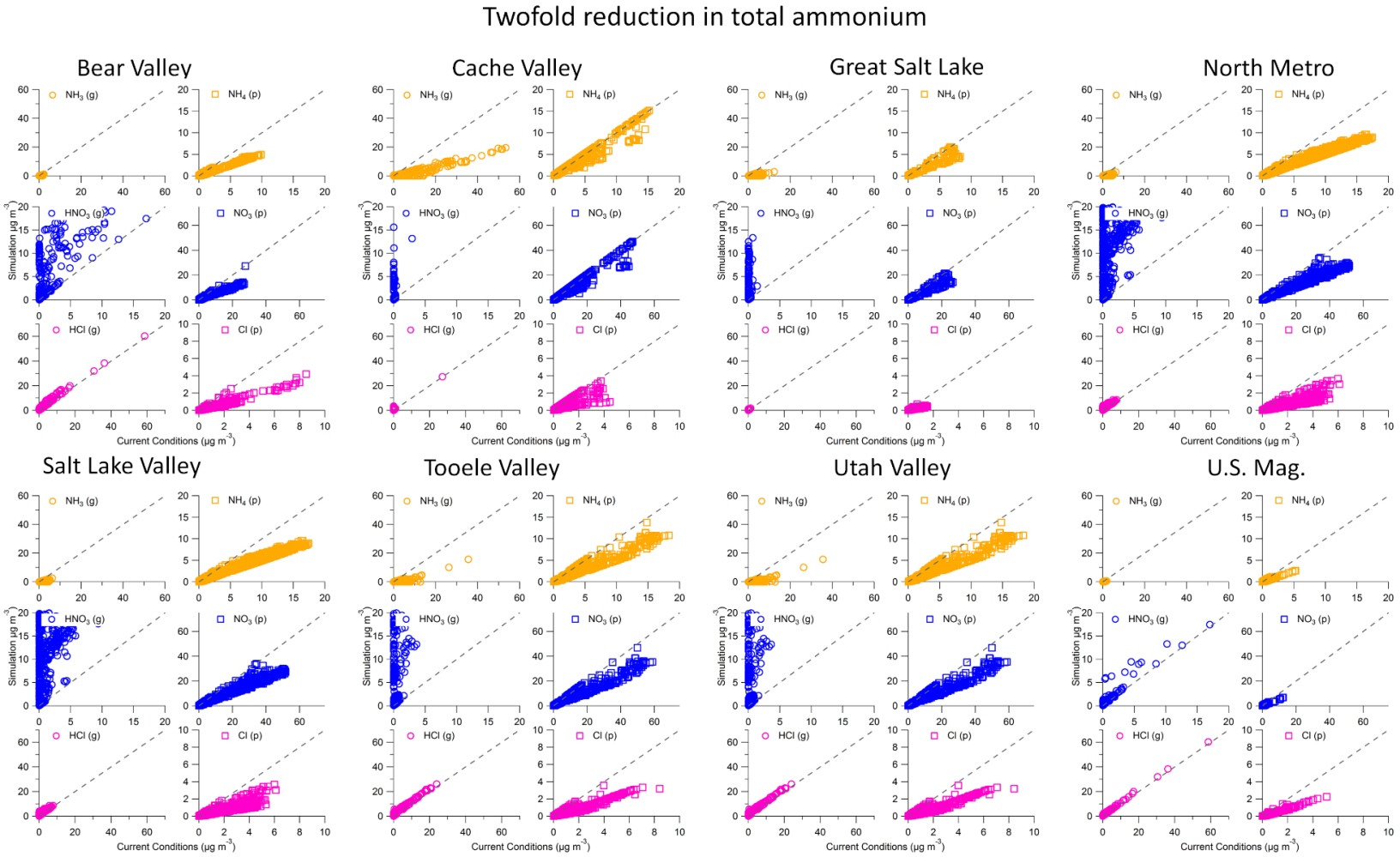

Figure S10. ISORROPIA model outputs of inorganic species for simulations using 50% decreases in total ammonium inputs from the UWFPS measurements (y-axis) compared to the corresponding model outputs using the current measured inputs (x-axis). For each location, the data are plotted in the same way as for Figure S10 (i.e., gas phase in the left column and particle phase in the right column, with ammonium, nitrate and chloride species in yellow, blue and pink, respectively).

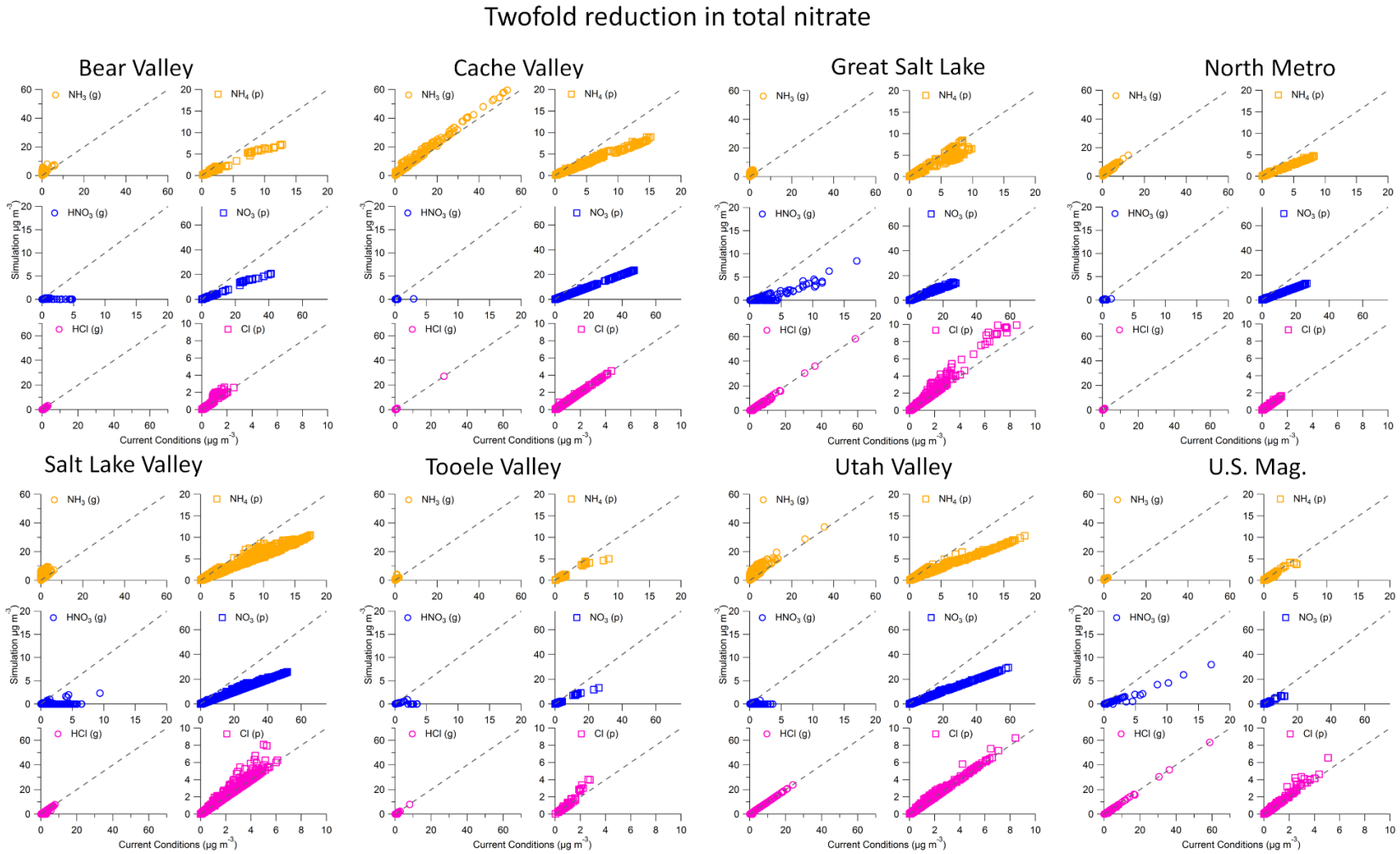

Figure S11. Same as for Figure S11, except the simulations are using 50% decreases in total nitrate inputs instead of decreases in total ammonium inputs. All locations respond to a decrease in total nitrate, indicating that inorganic aerosol formation in the region is predominantly nitrate limited.

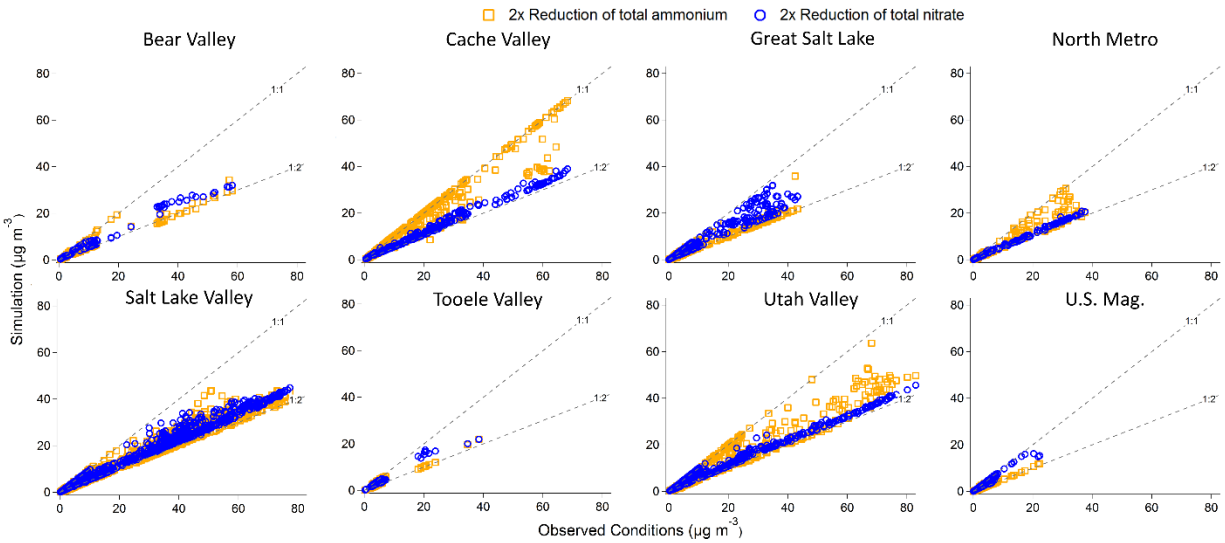

Figure S12 Comparison of the current total inorganic aerosol mass (x-axis) and the total inorganic aerosol mass simulated using ISORROPIA (y-axis). Same as Figure 11 in the main text, but shown for all the locations.

Table S1. Coefficient values for the linear regressions shown in figure S9

Chemical Species	Coefficient values				
	a	b	σ_a	σ_b	r^2
NH3	-0.14	1.023	0.01	0.003	0.983
HNO3	0.00	0.892	0.03	0.019	0.555
HCl	-0.86	0.927	0.02	0.004	0.962
NH4+	0.36	0.941	0.02	0.002	0.985
NO3-	-0.11	1.013	0.02	0.001	0.997
Cl-	0.95	1.203	0.03	0.056	0.161

References:

Allan, J. D., et al. (2003), Quantitative sampling using an Aerodyne aerosol mass spectrometer 2. Measurements of fine particulate chemical composition in two U.K. cities, *J. Geophys. Res.*, *108*(D3), 4091.

Allan, J. D., et al. (2004), A generalised method for the extraction of chemically resolved mass spectra from Aerodyne aerosol mass spectrometer data, *Journal of Aerosol Science*, *35*(7), 909-922.

Bahreini, R., J. L. Jimenez, J. Wang, R. C. Flagan, J. H. Seinfeld, J. T. Jayne, and D. R. Worsnop (2003), Aircraft-based aerosol size and composition measurements during ACE-Asia using and Aerodyne aerosol mass spectrometer, *J. Geophys. Res.*, *108*(D23), 8645, doi: 8610.1029/2002JD003226.

Bahreini, R., E. J. Dunlea, B. M. Matthew, C. Simons, K. S. Docherty, P. F. DeCarlo, J. L. Jimenez, C. A. Brock, and A. M. Middlebrook (2008), Design and operation of a pressure-controlled inlet for airborne sampling with an aerodynamic aerosol lens, *Aerosol Sci. Technol.*, *42*(6), 465-471.

Canagaratna, M. R., et al. (2007), Chemical and microphysical characterization of ambient aerosols with the Aerodyne aerosol mass spectrometer, *Mass Spectrometry Reviews*, *26*(2), 185-222.

DeCarlo, P. F., J. G. Slowik, D. R. Worsnop, P. Davidovits, and J. L. Jimenez (2004), Particle morphology and density characterization by combined mobility and aerodynamic diameter measurements. Part 1: Theory, *Aerosol Sci. Technol.*, *38*(12), 1185–1205.

Jayne, J. T., D. C. Leard, X. Zhang, P. Davidovits, K. A. Smith, C. E. Kolb, and D. R. Worsnop (2000), Development of an aerosol mass spectrometer for size and composition analysis of submicron particles, *Aerosol Science and Technology*, *33*(1-2), 49-70.

Liao, J., C. A. Brock, D. M. Murphy, D. T. Sueper, A. Welti, and A. M. Middlebrook (2017), Single-particle measurements of bouncing particles and in situ collection efficiency from an airborne aerosol mass spectrometer (AMS) with light-scattering detection, *Atmospheric Measurement Techniques*, *10*, 1-20.

Matthew, B. M., A. M. Middlebrook, and T. B. Onasch (2008), Collection efficiencies in an Aerodyne aerosol mass spectrometer as a function of particle phase for laboratory generated aerosols, *Aerosol Science and Technology*, *42*(11), 884-898.

Middlebrook, A. M., R. Bahreini, J. L. Jimenez, and M. R. Canagaratna (2012), Evaluation of composition-dependent collection efficiencies for the Aerodyne aerosol mass spectrometer using field data, *Aerosol Science and Technology*, *46*(3), 258-271.

Perry, R. H., and D. W. Green (Eds.) (1997), *Perry's Chemical Engineers' Handbook*, Table 2-37 pp., McGraw-Hill, New York, NY.

NIST Chemistry WebBook (https://webbook.nist.gov/chemistry/) last accessed July 2018